

Supplementary Materials for

***Bacillus subtilis* SMC complexes juxtapose chromosome arms as they travel from origin to terminus**

Xindan Wang,* Hugo B. Brandão, Tung B. K. Le, Michael T. Laub, David Z. Rudner*

*Corresponding author. Email: rudner@hms.harvard.edu (D.Z.R.); xindan@indiana.edu (X.W.)

Published 3 February 2017, *Science* **355**, 524 (2017)
DOI: 10.1126/science.aai8982

This PDF file includes:

Materials and Methods
Figs. S1 to S11
Tables S1 to S3
References

Materials and Methods

General methods

Bacillus subtilis strains were derived from the prototrophic strain PY79 (25). Cells were grown in defined rich medium (CH) (26) at 37°C. The generation time in this medium ranged from 34 to 44 minutes. Strains harboring single *parS* sites near the terminus grew slower than those with origin-proximal *parS* sites. Lists of strains, plasmids and oligonucleotides are available in Tables S1-S3.

Hi-C

The detailed Hi-C protocol was described in Wang et al, 2015 (4). Briefly, cells were crosslinked with 3% formaldehyde at room temperature for 30 min then quenched with 125 mM glycine for 5 min. 5×10^7 cells were used for each Hi-C reaction. Cells were lysed using Ready-Lyse Lysozyme (Epicentre, R1802M) followed by 0.5% SDS treatment. Solubilized chromatin was digested with HindIII for 2 hrs at 37°C. The cleaved ends were filled in with Klenow and Biotin-14-dATP, dGTP, dCTP, dTTP. The products were then ligated with T4 DNA ligase overnight at 16°C. Crosslinking was reversed at 65°C overnight in the presence proteinase K. The DNA was then extracted twice with phenol/chloroform/isoamylalcohol (25:24:1) (PCI), precipitated with ethanol, and resuspended in 20 μ l of QIAGEN EB buffer. Biotin from non-ligated ends was removed using T4 polymerase (4 hrs at 20°C) followed by extraction with PCI. The DNA was then sheared by sonication in 10s on / 10s off cycles for 12 min with 60% amplitude using a Qsonica Q800 water bath sonicator. The sheared DNA was used for library preparation with the NEBNext Ultra kit (E7370S) according to the manufacturer's instructions for end repair, adapter ligation, and size selection. Biotinylated DNA fragments were purified using 10 μ l streptavidin beads. 5 μ l DNA-bound beads were used for PCR in a 50 μ l reaction for 14 cycles. PCR products were purified using Ampure beads and sequenced at the Tufts core facility using HiSeq 2500.

Generation of Hi-C contact maps

Paired-end sequencing reads were mapped to the genome of *B. subtilis* PY79 (NCBI Reference Sequence NC_022898.1) using the same pipeline described in Wang et al., 2015 (4). The genetic loci marked by degree ($^\circ$) were calculated using the PY79 genome, which results in a slight shift from data published using *B. subtilis* 168 genomic coordinates. The *B. subtilis* PY79 genome was first divided into 404 10-kb bins. The interaction matrices were generated, and normalized using an iterative normalization procedure, implemented using the hiclib library for Python (<https://bitbucket.org/mirnylab/hiclib>) (4, 19, 27). Subsequent analysis and visualization were done using R scripts or MATLAB 8.5 (R2015) (MathWorks, Natick, MA). For presentation, the circular genome was linearized either at the replication terminus to generate origin-centered contact maps, or linearized at the replication origin to generate terminus-centered contact maps, as specified in each figure.

Mapping endpoints of DNA juxtaposition on Hi-C maps

To determine the extent of DNA incorporated into the zip-up (Figures 1, 2 and S10), a three-step process was used. First, the mean and standard deviation (σ) of contact

probabilities for each Hi-C map were computed. To minimize biases to the estimates of the mean and standard deviation (σ) from contributions arising from chromosome features like condensin-dependent interactions, we used robust statistics: as an estimate of the mean, we calculated the median; and as an estimate of the standard deviation, we calculated the median absolute deviation and multiplied it by 1.4826 (28). The contact probabilities equal to 0.50x, 0.75x, 1.00x, or 1.25x standard deviations (σ) above the mean were set as the threshold values. Next, interaction probabilities above or below the threshold were assigned a value of 1 or 0 respectively, generating an enrichment map with a binary profile showing points with a Hi-C score above the specified threshold (Figure S2, left panels, points in light green and yellow). Lastly, a point-connecting algorithm was employed to identify the largest contiguous region of enrichment (Figure S2, left panels, highlighted in yellow) after applying a mask of 30-35 bins (300-350 kb) to remove contributions arising from the primary diagonal that represents short-range interactions along the chromosome arms.

Lastly, to avoid missing entire sections of connected segments, especially at higher threshold values, we chose to connect neighbors separated by as many as 15 unconnected bins (150 kb). This was performed by the “imclose()” function in MATLAB 8.5 (R2015) using a diamond structuring element with a radius specified in each figure. From this contiguous region, the coordinates of the maximum excursion away from the *parS* site were obtained (white dotted lines), and labeled on the Hi-C contact maps (Figure S2, right panels, blue dotted lines). For consistency throughout the study, the measurements using a threshold of 1.0x σ (1 standard deviation above the mean) were reported in the main text.

Calculating rates of DNA juxtaposition

The rates of DNA juxtaposition were calculated from a linear fit to “the position versus time” plots, where position was the “endpoint of DNA juxtaposition” determined as described above. The reported rates and their errors were calculated from the slope of the line of best fit and the standard error of the regression, respectively. In Figure S10 and S11, we observed that the rate of DNA juxtaposition in the region origin-proximal to *parS* was bi-phasic. We therefore calculated the rates independently using the first two time points and separately the last 4 time points.

ChIP-seq

Chromatin immunoprecipitation (ChIP) was performed as described previously (4). Briefly, cells were crosslinked using 3% formaldehyde for 30 min at room temperature and then quenched, washed, and lysed. Chromosomal DNA was sheared to an average size of 250 bp by sonication using a Qsonica Q800 water bath sonicator. The lysate was then incubated overnight at 4°C with anti-SMC (29), anti-ParB (30), anti-ScpA, anti-ScpB, anti-GFP (31) or anti-FtsZ (32) antibodies, and was subsequently incubated with Protein A-Sepharose resin (GE HealthCare) for 1 hr at 4°C. After washes and elution, the immunoprecipitate was incubated at 65°C overnight to reverse the crosslinks. The DNA was further treated with RNaseA, Proteinase K, extracted using PCI, resuspended in 50 µl EB and used for library preparation with the NEBNext Ultra kit (E7370S) and sequenced using the Illumina MiSeq platform.

Anti-ScpA and anti-ScpB antisera were generated using recombinant ScpA-(His)₆ and (His)₆-ScpB expressed in and purified from *E. coli* BL21 DE3 pLysS. Peak fractions from Ni²⁺-affinity chromatography were used to generate polyclonal antibodies in rabbit (Covance).

Generation of ChIP-seq plots

The sequencing reads from ChIP and input samples were mapped to *B. subtilis* PY79 genome (NCBI Reference Sequence: NC_022898.1) using CLC Genomics Workbench (CLC bio, QIAGEN). Subsequent normalization, plotting, and analyses were done using R plots as follows. Every sample was first normalized to the total number of reads. Then ChIP enrichment was obtained by calculating the ratio of ChIP signal relative to Input (ChIP/Input). For some analyses, after these normalizations, a ratio between the ChIP enrichment of two samples was plotted, either in linear scale or in log₂ scale, as specified in each figure. The data were plotted in 1 kb windows, except for log₂(ratio) plots, which were in 5 kb windows. For presentation purposes, the x-axis was either origin-centered or terminus-centered as specified.

Calculating the endpoints of ChIP enrichment

To analyze SMC enrichment endpoints in strains with a single *parS* site at -59°, -94°, -117° or -153° in Figure 2B and Figure S4B, anti-SMC ChIP enrichment from a strain lacking *parS* sites (Figure S3B) was used as a baseline of SMC enrichment. The ratios of ChIP enrichment from strains that harbor a *parS* site (Figure 2B, Figure S4B) relative to this baseline were plotted in a log₂ scale in 5 kb bins (see Figure S6A). Values above 0 indicate higher SMC enrichment in the strain with a *parS* site than in a strain without *parS* sites, while values below 0 indicate lower SMC enrichment in strain with a *parS* site than in strain without *parS* sites. The endpoints of SMC enrichment were defined as the position at which the log₂(ratio) was 0.

To determine GFP-SMC enrichment endpoints upon IPTG induction in Figure 3, anti-GFP ChIP enrichment at time 0 (prior to induction) (Figure S8A, 2nd panel) was used as the baseline of GFP-SMC enrichment. The ratio of ChIP-seq enrichment from different time points relative to time 0 was plotted on a log₂ scale in 5 kb bins (see Figure S8D). The endpoints of GFP-SMC enrichment were defined as the position at which the log₂(ratio) was 0.

Immunoblot analysis

Immunoblot analysis was performed as described previously (4). Cells were collected and resuspended in lysis buffer [20 mM Tris pH 7.0, 10 mM EDTA, 1 mg/ml lysozyme, 10 µg/ml DNase I, 100 µg/ml RNase A, with protease inhibitors: 1 mM PMSF, 1 µg/ml leupeptin, 1 µg/ml pepstatin] to a final OD₆₀₀ of 10 for equivalent loading. The cells were incubated at 37°C for 10 min followed by addition of equal volume of sodium dodecyl sulfate (SDS) sample buffer [0.25 M Tris pH 6.8, 4% SDS, 20% glycerol, 10 mM EDTA] containing 10% 2-Mercaptoethanol. Samples were heated for 5 min at 80°C prior to loading. Proteins were separated by SDS-PAGE on 10% (for anti-SMC and anti-SigA) or 15% (for anti-ParB, anti-ScpA, and anti-ScpB)

polyacrylamide gels, electroblotted onto Immobilon-P membranes (Millipore) and blocked in 5% nonfat milk in phosphate-buffered saline (PBS)-0.5% Tween-20. The blocked membranes were probed with anti-GFP (1:10,000) (31), anti-ParB (1:5,000) (30), anti-SMC (1:5000) (29), anti-SigA (1:10,000) (33), anti-ScpA (1:10,000), or anti-ScpB (1:10,000) diluted into 3% BSA in 1x PBS-0.05% Tween-20. Primary antibodies were detected using horseradish peroxidase-conjugated goat anti-rabbit IgG (BioRad) and the Super Signal chemiluminescence reagent as described by the manufacturer (Pierce). The signal was captured using Bio-Rad ChemiDoc XRS and the intensity of each band was quantified using ImageLab 3.0 software (BioRad).

Microscopy

Fluorescence microscopy was performed on a Nikon Ti microscope equipped with Plan Apo 100x/1.4NA phase contrast oil objective and a CoolSnapHQ² camera. Cells were immobilized using 2% agarose pads containing growth media. Membranes were stained with FM4-64 (Molecular Probes) at 3 µg/ ml. DNA was stained with DAPI at 2 µg/ml. Images were cropped and adjusted using MetaMorph software (Molecular Devices).

Plasmid construction

pWX707 [*amyE::Pspank (natRBS) gfp-smc (spec)*] was constructed by inserting *gfp-smc* containing the native ribosomal binding site (*natRBS*) of the *smc* gene (amplified from pKM287 (14) using oWX1466 and oWX517 and digested with XbaI and SphI) into pDR110 between NheI and SphI. pDR110 [*amyE::Pspank (spec)*] is an ectopic integration vector with an IPTG-inducible promoter (D.Z.R. unpublished).

Strain construction

-1°parS no a.b.. This strain (BWX3370) was built by introducing the -1° *parS* site, which is the wild-type *parS* site in *parB*, back to *parSΔ9* (BWX3212) (4). First, in the wild-type cells, a *loxP-spec-loxP* cassette was inserted downstream of the *parB* gene to link the wild-type *parS* site to *spec* cassette using isothermal assembly. The isothermal assembly reaction contained 3 PCR products: 1) a region containing *parAB* genes (amplified from wild-type genomic DNA using oWX507 and oWX1077); 2) *loxP-spec-loxP* cassette (amplified from pWX466 using universal primers oWX438 and oWX439) and 3) the region downstream of *parB* (amplified from wild-type genomic DNA using primers oWX1078 and oWX888). The transformants were amplified using oWX507 and oWX888 and sequenced using oWX507, oWX536 and oWX889. The genomic DNA from the resultant strain (BWX2614) was used to transform *parSΔ9*, resulting in BWX3272 (*parSΔ9 no a.b.*, -1° *parS loxP-spec-loxP*). The *loxP-spec-loxP* cassette was subsequently looped out using a *cre*-expressing plasmid pWX496, which contains a kanamycin resistance gene and a temperature sensitive replication origin, generating an unmarked strain containing a single *parS* site at -1° (BWX3370, *parSΔ9 no a.b.*, -1° *parS no a.b.*). The *parS* site was verified by sequencing the *parAB* region using oWX507, oWX536 and oWX889.

-59°parS loxP-kan-loxP. The +4° *parS* sequence (TGTTACACGTGAAACA) was inserted at -59° (in the intergenic region between *yvdB* and *yvdC*). An isothermal

assembly product was directly transformed to *parS Δ 9* (BWX3212) (4), which has all the 9 *parS* sites deleted from the *B. subtilis* genome. The isothermal assembly reaction contained 3 PCR products: 1) a region containing *yvdB* gene (amplified from wild-type genomic DNA using oWX1273 and oWX1274); 2) *loxP-kan-loxP* cassette flanked by the +4° *parS* sequence (amplified from pWX470 using universal primers oWX1241 and oWX438) and 3) the region containing *yvdC* (amplified from wild-type genomic DNA using primers oWX1275 and oWX1276). The transformants were amplified and sequenced using oWX1277 and oWX1278.

-94°parS no a.b.. Genomic DNA from BWX3217 (*parS Δ 8, -94°parS loxP-kan-loxP*) (4) was transformed to *parS Δ 9* (BWX3212) (4), to generate BWX3264 (*parS Δ 9 no a.b., -94°parS loxP-kan-loxP*). The *loxP-kan-loxP* cassette was subsequently looped out using a *cre*-expressing plasmid pDR244, which contains a spectinomycin resistance gene and a temperature sensitive replication origin, resulting in strain BWX3270 (*parS Δ 9 no a.b., -94°parS no a.b.*).

-117°parS loxP-kan-loxP. The +4° *parS* sequence (TGTTACACGTGAAACA) was inserted at -117° (in the intergenic region between *lysC* and *yslB*). An isothermal assembly product was directly transformed to *parS Δ 9* (BWX3212) (4). The isothermal assembly reaction contained 3 PCR products: 1) a region containing *lysC* gene (amplified from wild-type genomic DNA using oWX1285 and oWX1286); 2) *loxP-kan-loxP* cassette flanked by the +4° *parS* sequence (amplified from pWX470 using universal primers oWX1241 and oWX438) and 3) the region containing *yslB* (amplified from wild-type genomic DNA using primers oWX1287 and oWX1288). The transformants were amplified and sequenced using oWX1289 and oWX1290.

-153°parS loxP-kan-loxP. The +4° *parS* sequence (TGTTACACGTGAAACA) was inserted at -153° (in the intergenic region between *bmr* and *bmrR*). An isothermal assembly product was directly transformed to *parS Δ 9* (BWX3212) (4). The isothermal assembly reaction contained 3 PCR products: 1) a region containing *bmr* gene (amplified from wild-type genomic DNA using oWX1291 and oWX1292); 2) *loxP-kan-loxP* cassette flanked by the +4° *parS* sequence (amplified from pWX470 using universal primers oWX1241 and oWX438) and 3) the region containing *bmrR* (amplified from wild-type genomic DNA using primers oWX1293 and oWX1294). The transformants were amplified and sequenced using oWX1295 and oWX1296.

+26°parS loxP-kan-loxP. The +4° *parS* sequence (TGTTACACGTGAAACA) was inserted at +26° (in the intergenic region between *yccF* and *natK*). An isothermal assembly product was directly transformed to *parS Δ 9* (BWX3212) (4). The isothermal assembly reaction contained 3 PCR products: 1) a region containing *yccF* gene (amplified from wild-type genomic DNA using oWX1336 and oWX1337); 2) *loxP-kan-loxP* cassette flanked by the +4° *parS* sequence (amplified from pWX470 using universal primers oWX1241 and oWX438) and 3) the region containing *natK* (amplified from wild-type genomic DNA using primers oWX1338 and oWX1339). The transformants were amplified and sequenced using oWX1340 and oWX1341.

-27° *parS* no a.b. This strain (BWX3268) was built by deleting +91° *parS* site from *parS*Δ7 (BNS1615, N. Sullivan and D.Z.R unpublished), which is an intermediate strain towards building *parS*Δ8 (BNS1657) (14) and only contains the wild-type *parS* site at -27° and +91°. Genomic DNA from BWX3198 (4), which has the +91° *parS* site deleted and marked with *loxP-kan-loxP*, was transformed to BNS1615 to generate BWX3262 (*parS*Δ9 *loxP-kan-loxP*, -27° *parS* no a.b.). The *loxP-kan-loxP* cassette was subsequently looped out using a *cre*-expressing plasmid pDR244, which contains a spectinomycin resistance gene and a temperature sensitive replication origin.

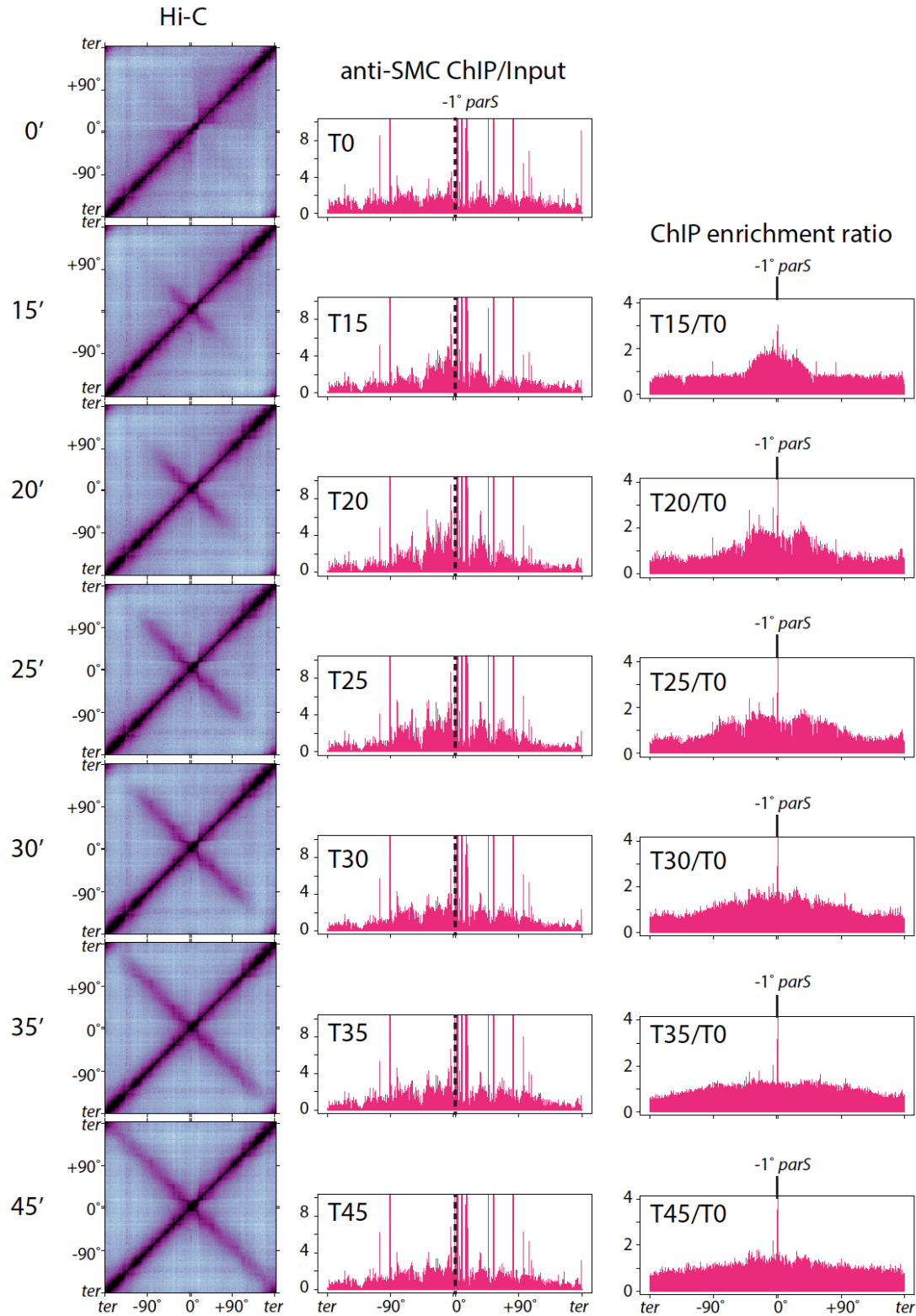
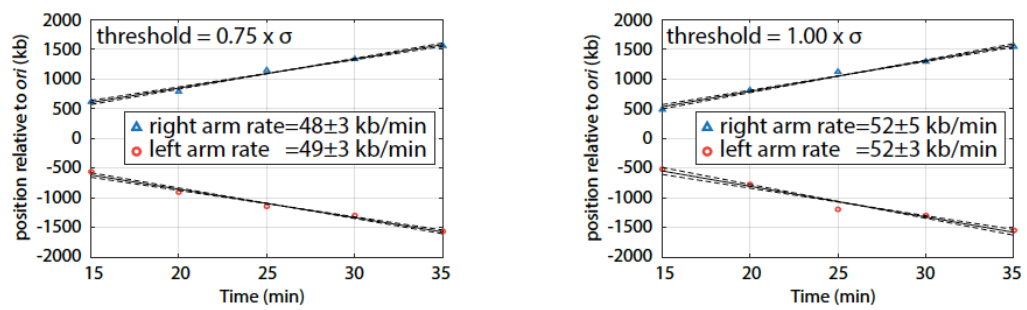
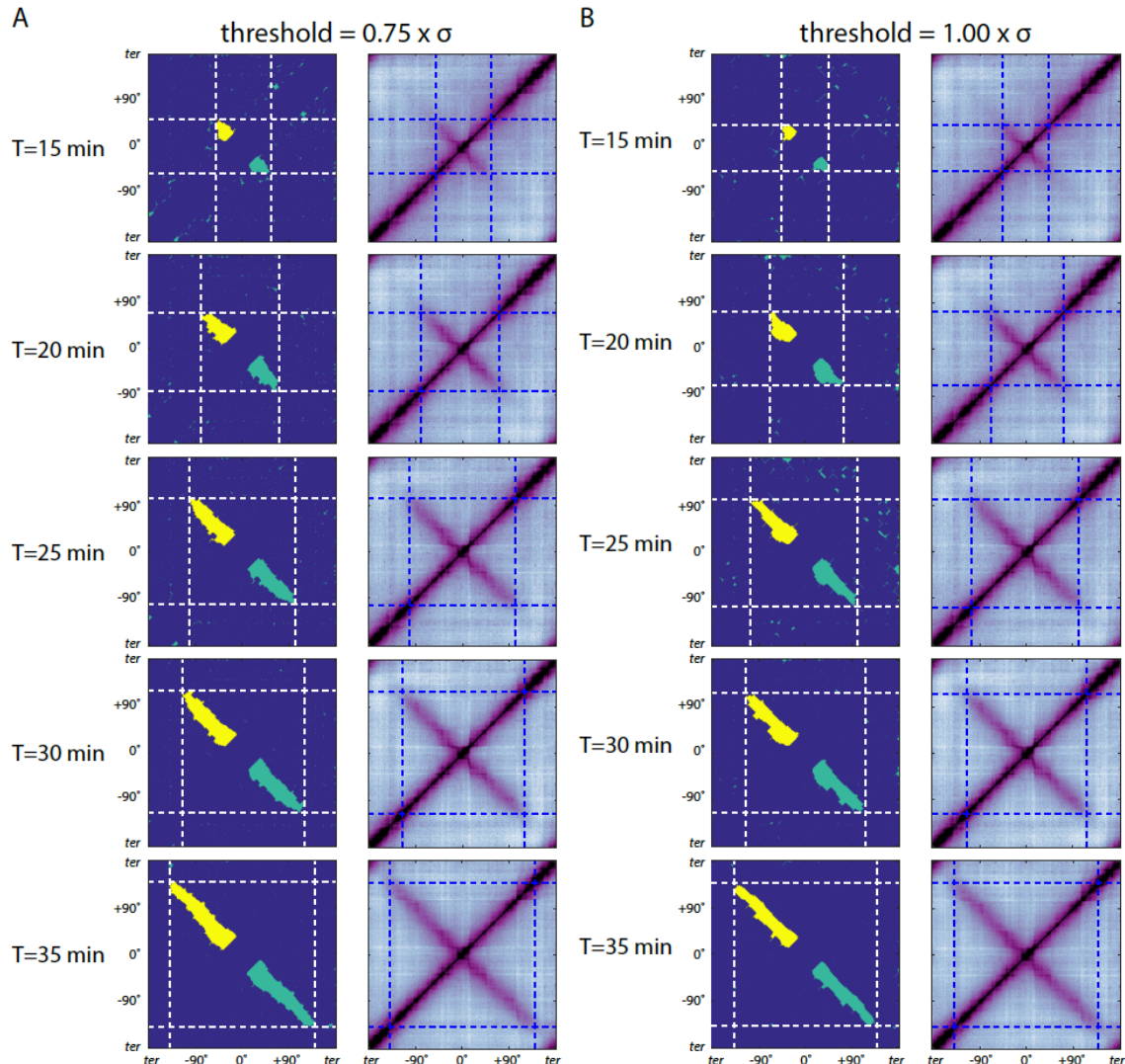


Fig. S1.

DNA juxtaposition propagates from the condensin loading site. Related to Figure 1.
Left column, normalized Hi-C contact maps for strain BWX3352, which harbors a single *parS* site at -1° and an IPTG-inducible *gfp-parB* fusion as the sole source of the ParB protein. GFP-ParB was induced with 1 mM IPTG for the indicated times (in minutes). The contact maps are oriented with the replication origin at the center. **Middle column**, ChIP enrichment profiles using anti-SMC antibodies from cells grown under the same condition as in the Hi-C experiments on the left. The sequencing reads were normalized to the total number of reads for each sample and mapped in 1 kb bins. The ratio of ChIP signal relative to input sample (ChIP enrichment) is shown. It is unclear whether SMC enrichment at the *rRNA* operons and other highly transcribed genes is specific (see Figure S3). **Right column**, the ratio of ChIP enrichment relative to time 0 (before induction) is plotted. The position of the *parS* site is indicated with black dotted lines on the plot (middle column) or black bars above the plot (right column).



C

threshold	right arm rate (kb/min)	left arm rate (kb/min)
$0.50 \times \sigma$	47 ± 3	48 ± 3
$0.75 \times \sigma$	48 ± 3	49 ± 3
$1.00 \times \sigma$	52 ± 5	52 ± 3
$1.25 \times \sigma$	51 ± 7	48 ± 10

Fig. S2.

Rate of DNA juxtaposition. Related to Figure 1. (A-B) The endpoints of DNA juxtaposition after GFP-ParB induction (from Fig. 1 and Fig. S1) were determined as described in Materials and Methods, using two thresholds: 0.75σ standard deviation (σ) above the mean Hi-C score in **(A)** and 1.0σ (**B**). Left panels, binary maps showing points (light green and yellow) with Hi-C interactions scores above the specified threshold. Neighboring points that were separated by less than 5 bins (50kb) (A), or 10 bins (100kb) (B) were connected. The largest region of inter-connected points (highlighted in yellow) was identified as the Hi-C enrichment region due to DNA juxtaposition. The endpoints of the Hi-C enrichment regions were identified (white dotted lines). For visualization, these positions were marked with blue dotted lines on the Hi-C contact maps in the right panels. The positions (relative to the replication origin) were plotted on the graphs at the bottom. An endpoint position on the right arm is labeled as a positive value, and on the left arm as a negative value. The rates and errors for the DNA juxtaposition were calculated from the slope of the line of best fit and the standard error of the regression, respectively. **(C)** Table of rates of DNA juxtaposition calculated from 4 different threshold values. The data highlighted in green (threshold= 1.0σ) are the measurements presented in the text.

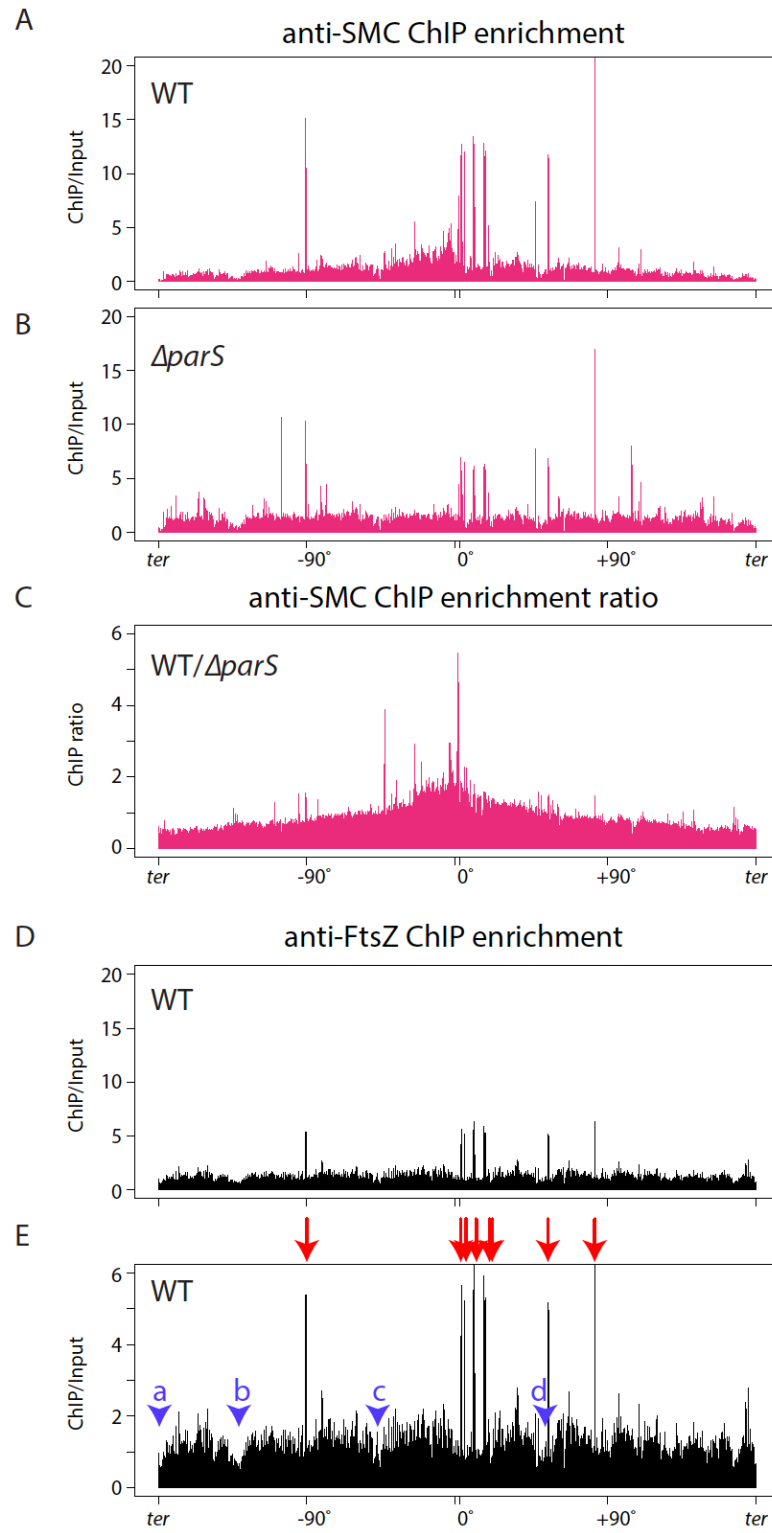


Fig. S3.

A shallow gradient of SMC enrichment from the replication origin to the terminus. (A-C) ChIP-seq profiles of SMC enrichment (using anti-SMC antibodies) in wild-type cells (A) or in cells lacking all 9 *parS* sites ($\Delta parS$) (B). The sequencing reads were normalized to the total number of reads for each sample and mapped in 1 kb bins. The ratio of ChIP signal relative to input sample (ChIP enrichment) is shown. A shallow gradient of SMC enrichment from the origin to the terminus is detected in wild-type but is absent in $\Delta parS$. To more clearly visualize the enrichment gradient, the ratio of ChIP enrichment in wild-type relative to $\Delta parS$ is plotted in (C). The plots are oriented with the origin at the center of the x-axis. (D-E) To control for non-specific enrichment, a ChIP-seq experiment using anti-FtsZ antibodies with wild-type cells is shown. The scale of the y-axis in (D) is the same as (A) and (B) for direct comparison. The scale in (E) is smaller to highlight features. FtsZ is not known to bind DNA, and (D) and (E) are representatives of a pattern observed in all ChIP-seq profiles in this study: (1) An increased number of reads (tall peaks highlighted with red arrows) that correspond to ribosomal RNA (*rrn*) operons and other highly transcribed genes (18). ChIP enrichment of loci containing highly transcribed genes has been reported previously (34-36). (2) Regions with reduced reads (4 examples highlighted by blue carets) with low levels of transcription (18). Region (a) is a ~30 kb region near the terminus (from +178° to -179°), from gene locus *pps* to *yobO*; region (b) is a ~100 kb region (from -131° to -140°), from *yraM* to *yqeF*; region (c) is a ~55 kb region (from -47° to -52°), from *ywtG* and *fliW*; and region (d) is a ~120 kb region (from 45° to 56°), from *ydcF* to *gutR*. Both patterns are consistent with the idea that formaldehyde more efficiently crosslinks single stranded DNA (37) and the process of transcription generates regions of ssDNA. Regions with reduced reads like the ones highlighted correlate with discontinuities in ChIP ratios between samples (Fig. S6A and S8D). We suspect that the low number of reads results in greater variability in ChIP enrichment between samples.

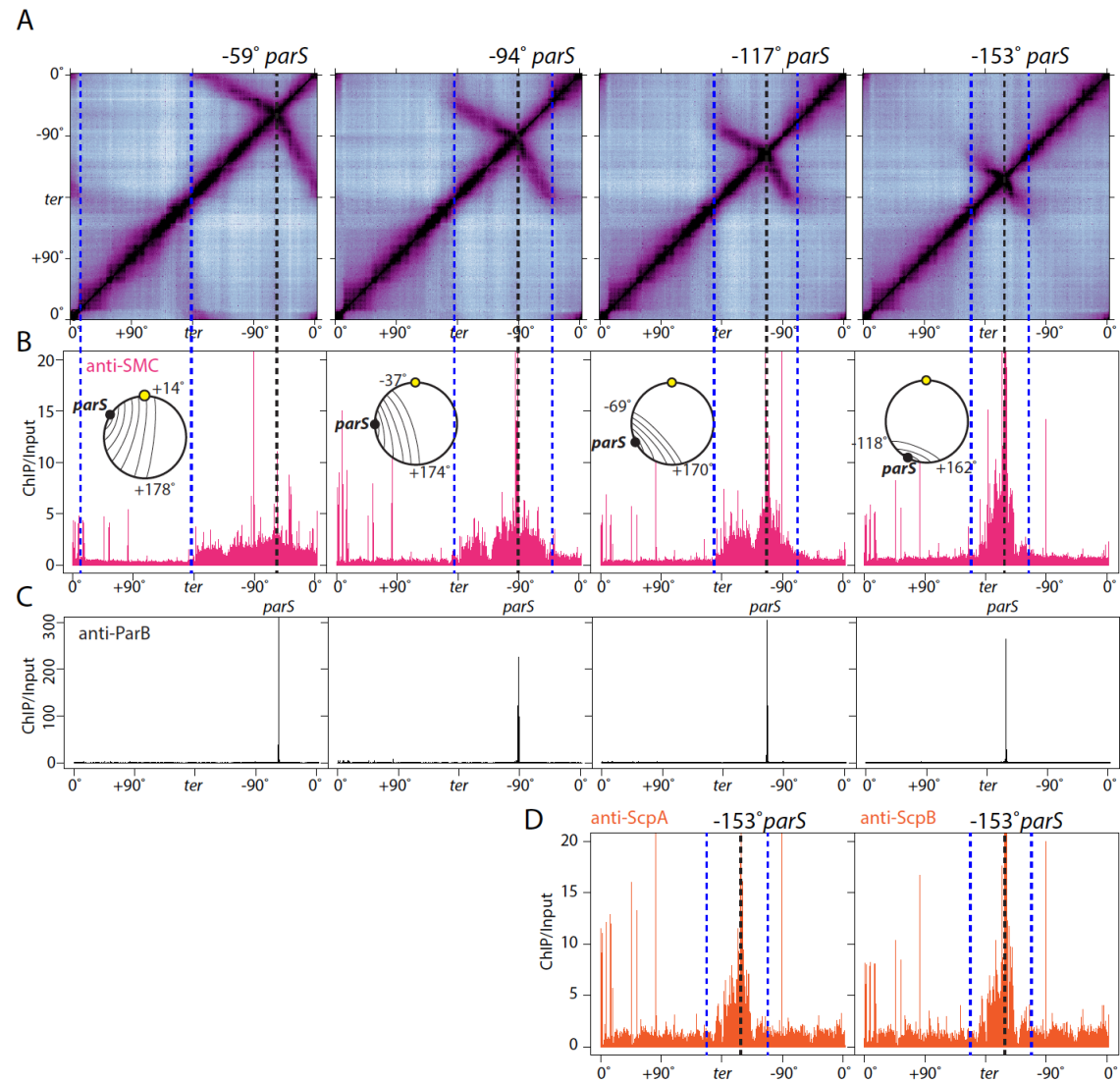


Fig. S4.

Condensin is specifically enriched along juxtaposed DNA. Related to Figure 2.

(A) Normalized Hi-C contact maps of strains harboring a single *parS* at -59° (BWX3377), -94° (BWX3270), -117° (BWX3381) and -153° (BWX3383). To more clearly visualize interactions in the terminus region, the maps were oriented with the terminus (*ter*) at the center and the origin (0°) at the periphery. The positions of the *parS* sites and the extent of DNA juxtaposition are indicated with black and blue dotted lines, respectively. Analysis to determine the extent of DNA juxtaposition can be found in Fig. S5 and is described in Materials and Methods. **(B)** ChIP-seq profiles of SMC enrichment. ChIP-seq (using anti-SMC antibodies) was performed on the same samples as in (A). Sequencing reads from ChIP and Input samples were normalized to the total number of reads for each sample and plotted in 1 kb bins. ChIP enrichment (the ratio of ChIP signal relative to Input) is presented. Schematic representations of the juxtaposition of DNA flanking the *parS* sites from the Hi-C matrices are shown. Analysis to determine the extent of SMC enrichment can be found in Fig. S6A. It is unclear whether SMC

enrichment at the *rRNA* operons and other highly transcribed genes outside the juxtaposed regions is specific (see Figure S3). **(C)** ChIP-seq profiles of ParB enrichment. ChIP-seq (using anti-ParB antibodies) was performed on the same samples as in (B). **(D)** ScpA and ScpB are enriched along the juxtaposed DNA flanking the *parS* site at -153°. ChIP-seq enrichment profiles from a strain harboring a single *parS* site at -153° (BWX3383) using anti-ScpA and anti-ScpB antibodies. The positions of the *parS* sites and the extent of DNA juxtaposition (A) are indicated with black and blue dotted lines, respectively.

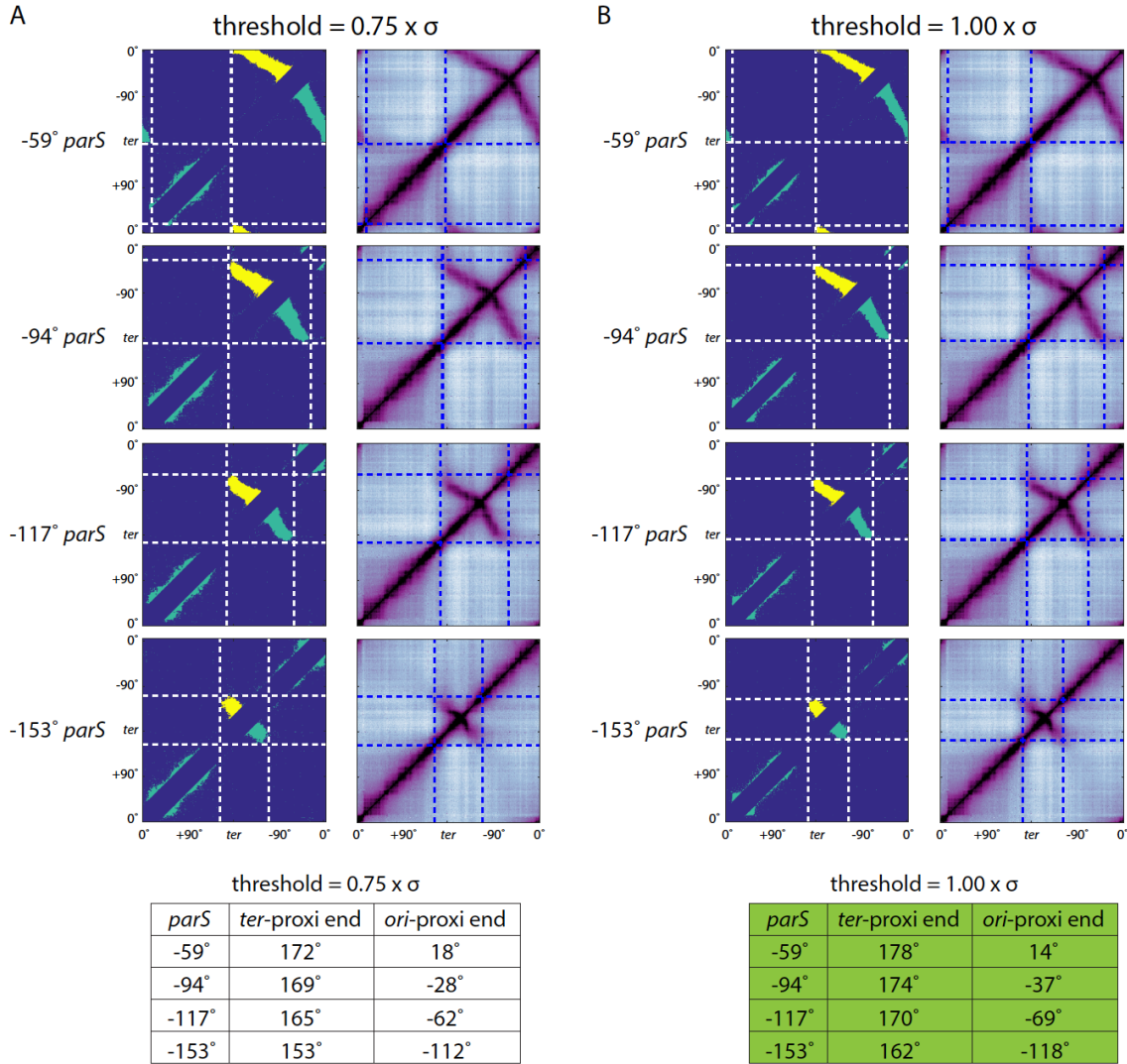


Fig. S5.

Determining the endpoints of DNA juxtaposition. Related to Figure 2. The endpoints of DNA juxtaposition in cells harboring a single *parS* site (Fig. 2A and S4) were determined as described in Materials and Methods, using thresholds of $0.75 \times \sigma$ (**A**) and $1.00 \times \sigma$ (**B**). Left panels, binary maps showing points (light green and yellow) with Hi-C interactions scores above the specified threshold. Neighboring points that were separated by less than 2 bins (20 kb) were connected. The largest region of connected points (highlighted in yellow) was identified as the Hi-C enrichment region due to DNA juxtaposition. The endpoints of the enrichment region were marked with white dotted lines. For visualization, these positions were marked with blue dotted lines on the Hi-C contact maps in the right panels. The measured positions of the endpoints (in degrees) are listed in the tables. The values used in the text (highlighted in green) were from (**B**), with the threshold set at 1 standard deviation (σ) above the mean.

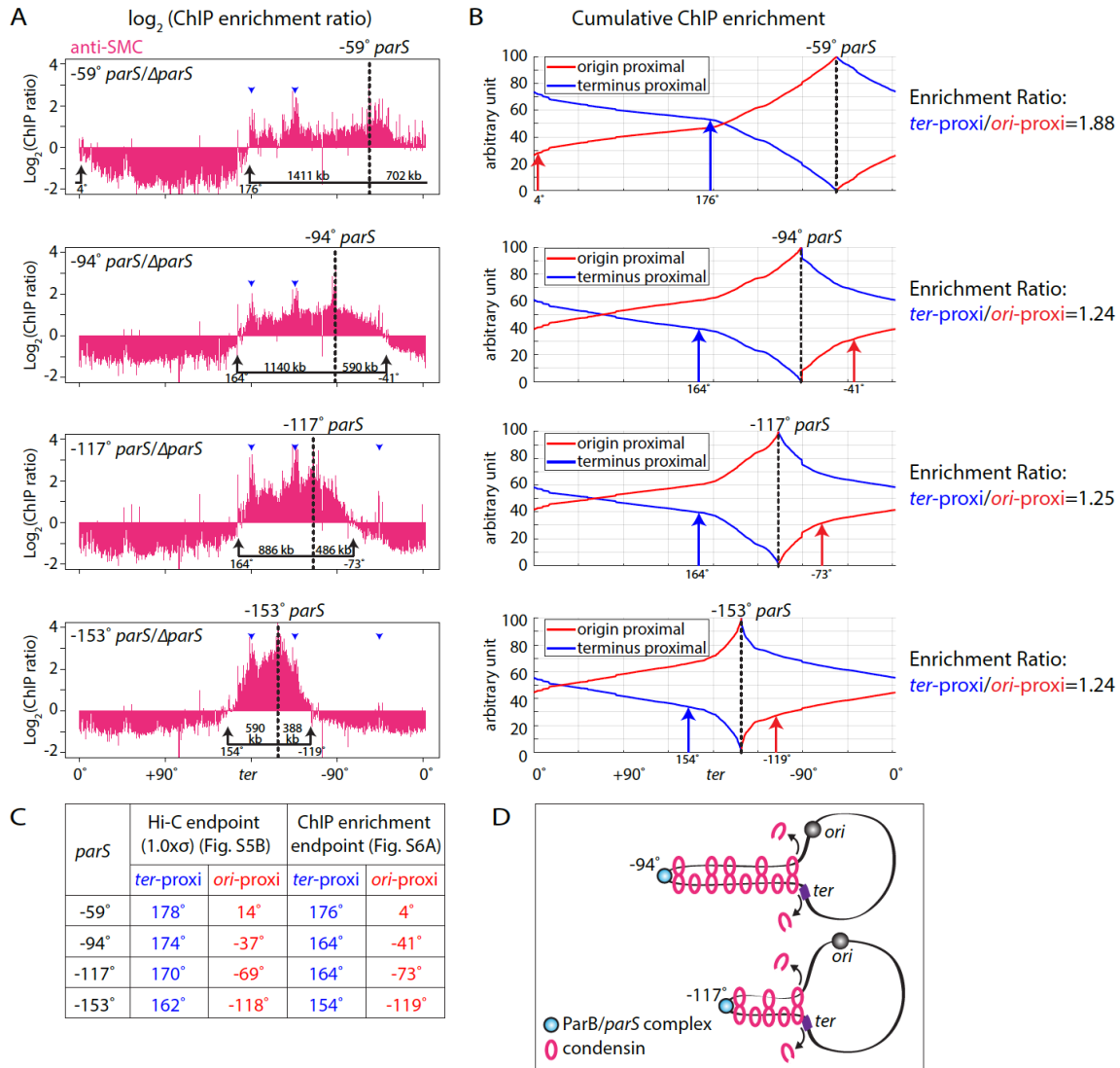


Fig. S6.

ChIP-seq analyses using anti-SMC antibodies. Related to Figure 2. (A) Analyses of SMC enrichment endpoints in strains with single *parS* sites at -59°, -94°, -117° and -153°. ChIP-seq reads from these strains were normalized to the total number of reads and to their corresponding input samples, to calculate ChIP enrichment (ChIP/Input). The ratios of ChIP enrichment of strains that harbor a *parS* site (Fig. 2B and S4B) relative to Δ *parS* (Fig. S3B) were plotted in log₂ scale in 5 kb bins. Black dotted lines indicate the positions of the *parS* sites. The SMC enrichment endpoints (black arrows) were defined as the position at which the log₂(ratio) was 0. The distances between each *parS* site and the ChIP enrichment endpoint are labeled. A detailed explanation of the analysis can be found in Materials and Methods. Blue carets highlight 3 regions in which there is a steep increase in ChIP ratio. These regions (+178° to -179°; -131° to -140°; and -47° to -52°) have reduced reads in all ChIP experiments (see Figure S3E, regions a, b and c). Accordingly, ratios of reads between experiments are more variable in these regions. (B) SMC is more enriched on the terminus-proximal side of *parS* than on the origin-proximal

side. The cumulative ChIP enrichments (ChIP/Input) in strains with single *parS* sites at -59°, -94°, -117° and -153° were calculated. Starting at the *parS* site, ChIP enrichment (from Fig. 2B and S4B) was summed upstream towards the origin (red lines) or downstream towards the terminus (blue lines). The arrows indicate the ChIP enrichment endpoints (along the x-axis) as determined in (A) on the origin-proximal side (red arrow) and terminus-proximal side (blue arrow) of *parS*. The y-axis values (in arbitrary units) represent the total ChIP enrichment between the *parS* site and the chromosomal position along the x-axis. The ratio of total terminus-proximal enrichment relative to total origin-proximal enrichment is indicated to the right of each plot. (C) Comparison of Hi-C DNA juxtaposition endpoints (Fig. S5B) and SMC ChIP enrichment endpoints in (A). The extent of DNA juxtaposition and SMC enrichment mapped within 10-110 kb of each other. (D) Schematic model based on the Hi-C and ChIP-seq data. Chromosomes with -94° *parS* site and separately -117° *parS* site are shown. Individual condensin rings (magenta) encircle DNA on either side of *parS* (blue) and tether the flanking DNA by interacting. Alternatively, condensin complexes could embrace the two duplexes such that individual rings encircle DNA on both sides of *parS* (not shown). Untethered rings on the terminus-proximal side of *parS* are included to reflect greater SMC enrichment on the terminus-proximal side of *parS* than the origin-proximal side as seen in (B). Since SMC does not appreciably accumulate at the ends of the zip-up, the condensin rings are shown disassociating in concert when the tethers reach the terminus region (purple).

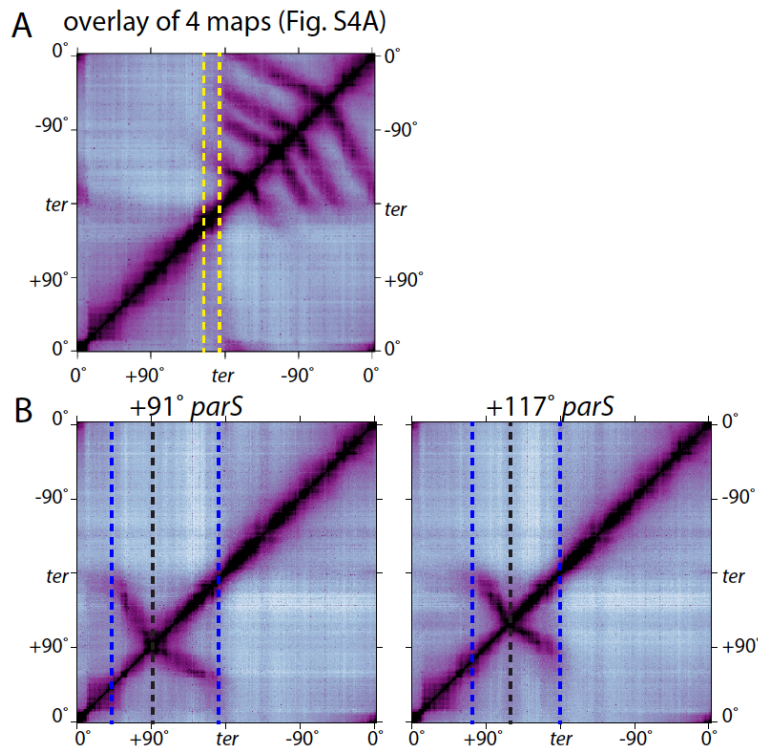


Fig. S7.

DNA juxtaposition does not extend beyond the terminus region. Related to Figure 2.

(A) Overlay of the four Hi-C contact maps shown in Fig. S4A. The extent of juxtaposition on the terminus-proximal side of the *parS* sites is indicated by yellow dotted lines. **(B)** Normalized Hi-C contact maps of strains harboring a single *parS* site on the right chromosome arm, at $+91^\circ$ and $+117^\circ$. The positions of the *parS* sites and the extent of juxtaposition are indicated with black and blue dotted lines, respectively.

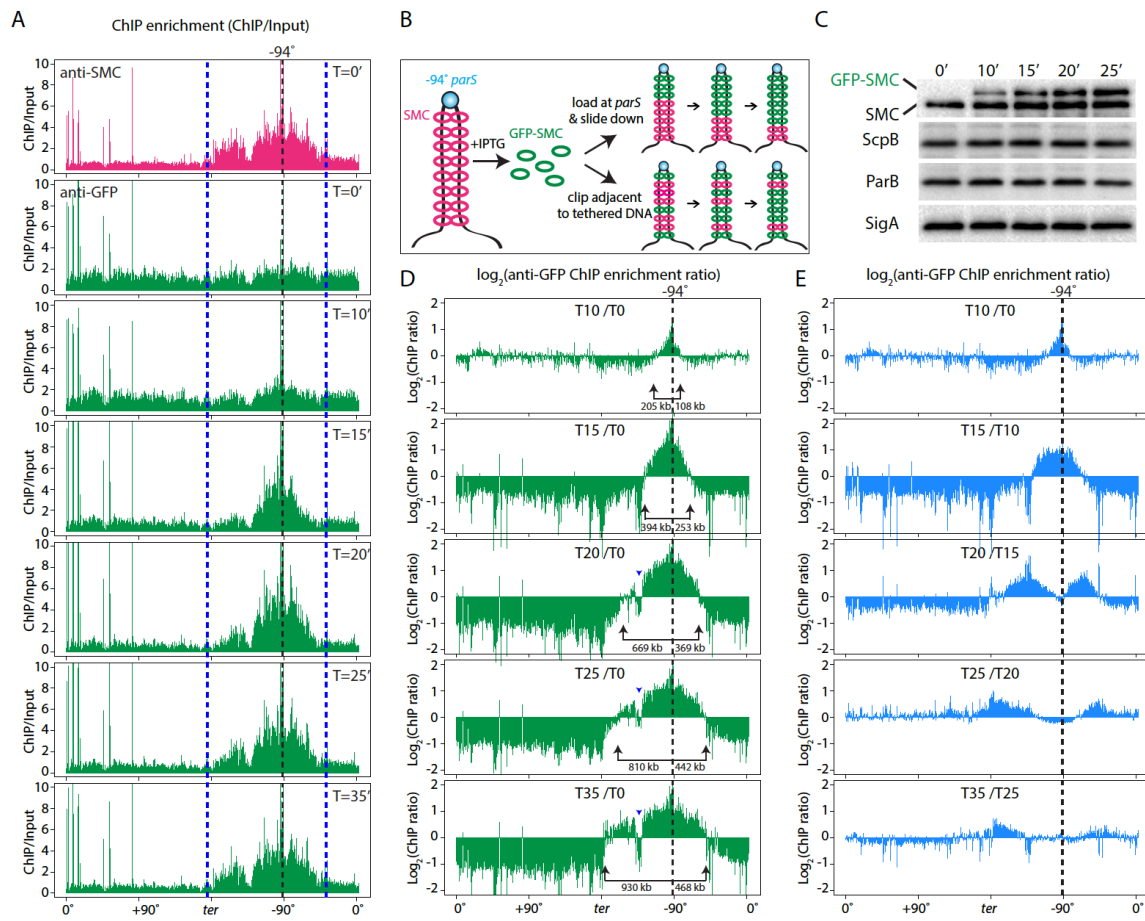


Fig. S8.

Condensin complexes loaded at *parS* travel down the flanking DNA. Related to Figure 3. (A) ChIP-seq enrichment profiles using anti-SMC antibodies at time 0, before the induction of a functional GFP-SMC fusion (top panel, magenta), or using anti-GFP antibodies at indicated times after IPTG induction (bottom panels, green). Cells (BWX3690) harbor a single *parS* site at -94°, wild-type *smc*, and an IPTG-inducible *gfp-smc* fusion. GFP-SMC was induced using 1 mM IPTG and cells were crosslinked and harvested at the indicated times after induction and subject to ChIP-seq using anti-GFP antibodies. Sequencing reads from ChIP and Input samples were normalized to the total number of reads at each time point. ChIP enrichment (the ratio of ChIP signal relative to the Input) is shown in 1 kb bins. Black dotted line indicates the position of the *parS* site, and blue dotted lines indicate the extent of ChIP enrichment of untagged SMC at time 0 (top panel). (B) Experimental set up to test two models for condensin accumulation along DNA flanking *parS*. If condensin loads at *parS* and travels down the chromosome arms (top) then condensin complexes containing newly synthesized GFP-SMC (green rings) will be enriched at *parS* and enrichment will progress away from *parS* over time. If condensin loads adjacent to tethered DNA (bottom) then condensin complexes containing newly expressed GFP-SMC will accumulate along the entire juxtaposed region. For simplicity, only the condensin rings containing GFP-SMC (green rings) are shown loaded after induction. Condensin tethers are drawn as handcuffs but could also function by embracing both DNA duplexes (not shown). (C) Immunoblot analysis of GFP-SMC

levels (using anti-SMC antibodies) during the induction time course. Time (in minutes) after IPTG addition is indicated. The levels of SMC, ScpB, and ParB were unchanged during the time course. SigA was used to control for loading. **(D)** Analyses of GFP-SMC enrichment endpoints. The ratios of ChIP enrichment at the indicated time point relative to time 0 (before induction) are shown in \log_2 scale in 5 kb bins. GFP-SMC enrichment endpoints were determined as described in Materials and Methods and in Fig. S6A. Black dotted lines indicate the position of the *parS* site. The distances between the *parS* site and the ChIP enrichment endpoints are labeled. The discontinuity in the $\log_2(\text{ChIP ratio})$ (blue carets) corresponds to a region that has fewer ChIP enrichment reads under all conditions (see Fig. S3E, region c). **(E)** GFP-SMC enrichment profiles in which the ratios of ChIP enrichment at the indicated time point relative to the previous time point was plotted in \log_2 scale in 5 kb bins. A value above 0 indicates more reads at a particular time point relative to the previous time point. The GFP-SMC enrichment profile follows a wave-like pattern emanating from *parS*. Since the cells used in these experiments contain constitutively expressed SMC (lacking GFP), the wave-like pattern reflects condensin complexes with newly synthesized GFP-SMC traveling away from the *parS* site. Finally, we note that since GFP-SMC travels towards the origin, the replisome cannot be the motive force for condensin movement.

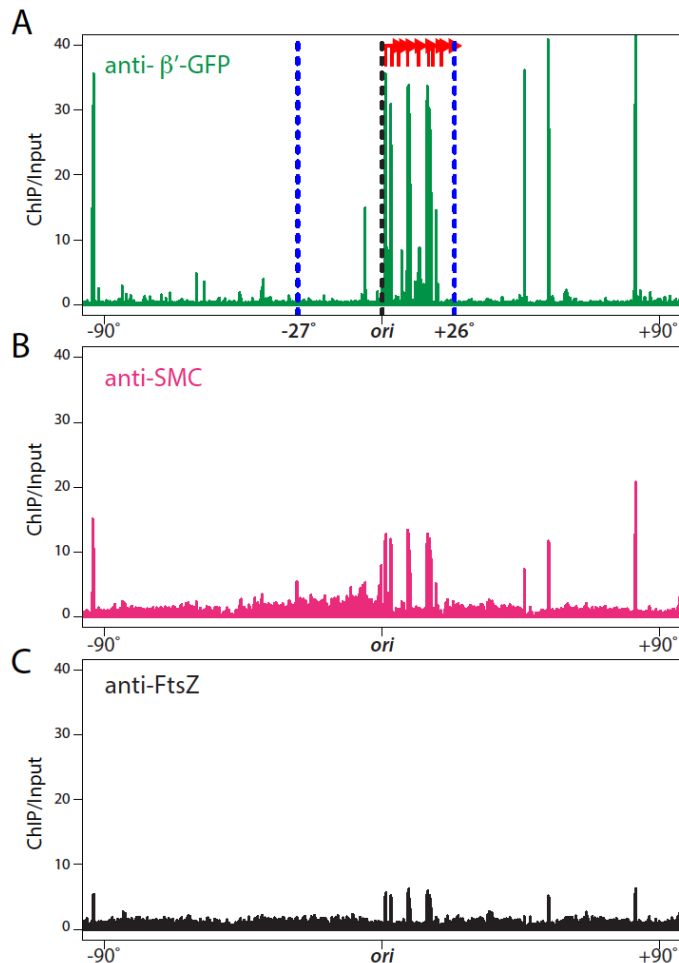


Fig. S9.

(A) RNA polymerase enrichment profile (using anti-GFP antibodies) in cells (BDR1841) harboring an RpoC-GFP (β' -GFP) fusion as the only source of RpoC. The position of the origin is labeled as a black dotted line, and the positions of +26° and -27° *parS* sites as blue dotted lines. The highly transcribed genes adjacent to the origin on the right arm are shown schematically as red arrows. All of these genes are on the leading strand. Since highly transcribed genes are prone to non-specific ChIP enrichment (Fig. S3DE), the ChIP profile of β' -GFP likely over-estimates β' -GFP enrichment at these positions and therefore only provides a qualitative view of RNA polymerase occupancy. **(B-C)** For comparison, ChIP-seq enrichment profiles using anti-SMC and anti-FtsZ antibodies in wild-type cells are plotted with the same scale.

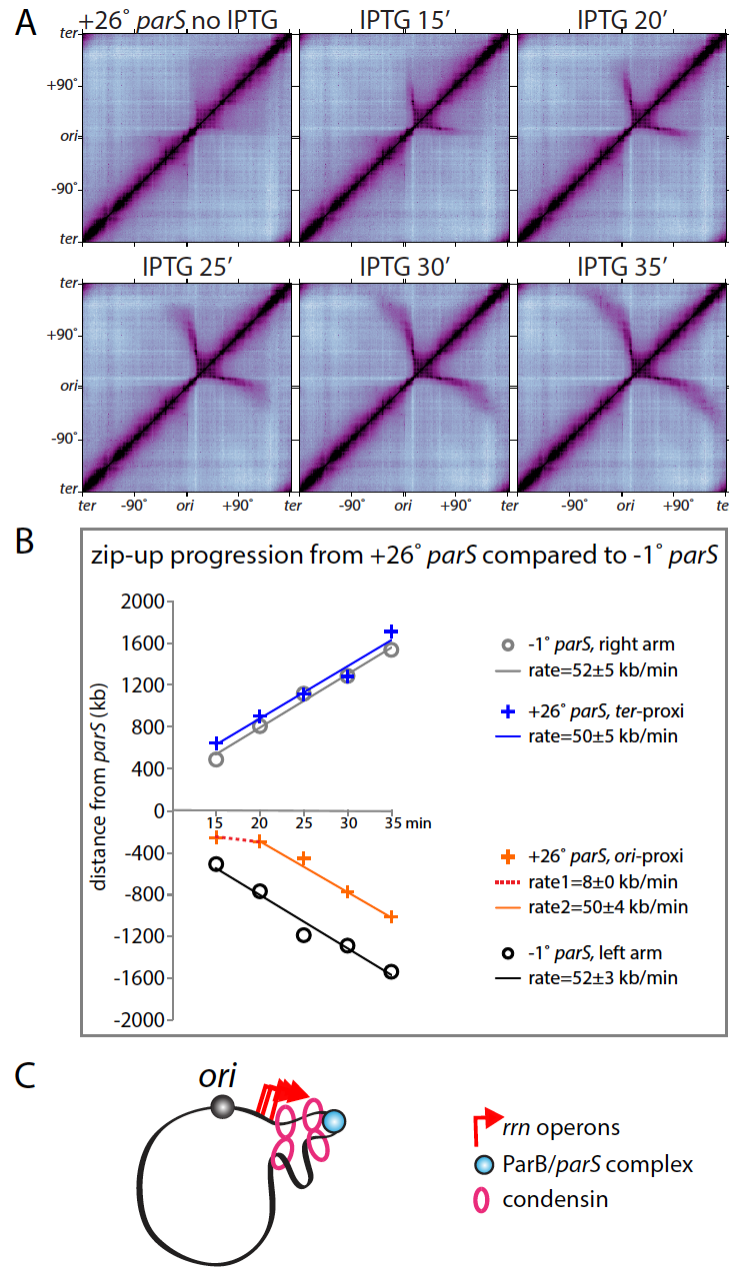


Fig. S10.

Differential rates of DNA juxtaposition. (A) Normalized Hi-C contact maps for strain BWX3596 harboring a single *parS* site at +26° and *gfp-parB* under IPTG control as the sole source of ParB. IPTG was added to a final concentration of 1 mM for the indicated amounts of time. The contact maps are oriented with the replication origin at the center of the axes. (B) Analysis of zip-up progression from the +26° *parS* site. The extent of DNA that was incorporated into the zip-up at the indicated time points in (A) was plotted for the origin-proximal region (orange) and terminus-proximal region (blue). Endpoint positions on the terminus-proximal side (clockwise from the *parS*) were given positive values, and on the origin-proximal side (counterclockwise from the *parS*) were given negative values. Analysis to determine the extent of DNA incorporation can be found in

Figure S11 and is described in Materials and Methods. For comparison, the zip-up progression from -1° *parS* site in Fig. S2B is re-plotted. Endpoint positions on the right arm (clockwise from the *parS*) were given positive values, and on the left arm (counterclockwise from the *parS*) negative values. The rates of zip-up are indicated. **(C)** Schematic model that accounts for the different rates of juxtaposition. Condensin rings (magenta) are shown as handcuffs, ParB/*parS* as a light blue ball, and the highly transcribed genes adjacent to the origin as red arrows. When a condensin ring traveling toward the origin encounters the highly transcribed gene cluster (red arrows), its movement is impaired. The partner ring traveling toward the terminus is unimpeded and moves at rates similar to tethers loaded at the origin. As a consequence of this differential movement, a small region of origin-proximal DNA interacts with a much larger region of terminus-proximal DNA. A single condensin ring that encircles both DNA duplexes flanking *parS* could also generate this interaction pattern. However, it would require that the traffic from the highly transcribed genes would only impact movement of one of the two duplexes through the shared pore of the ring.

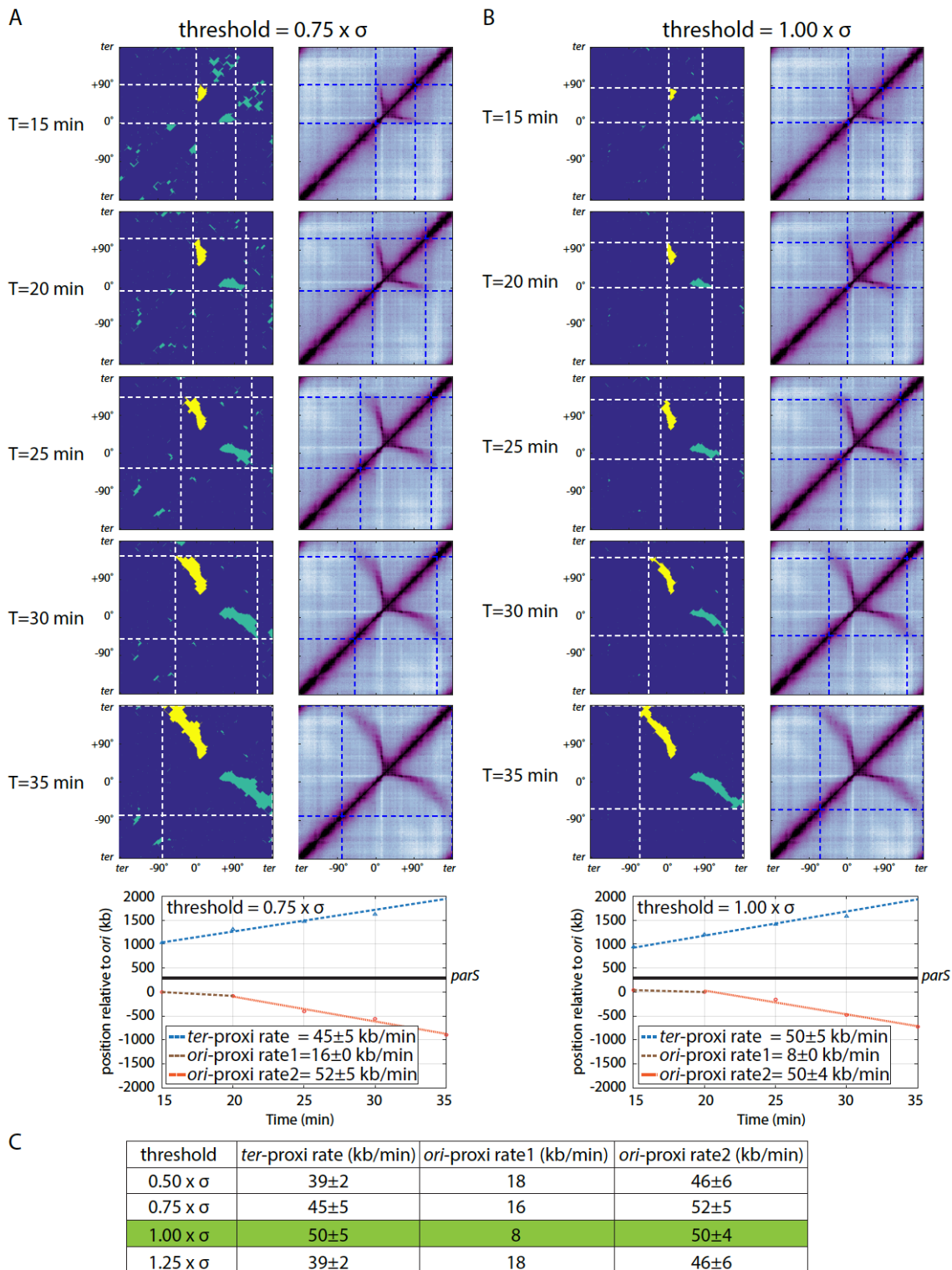


Fig. S11.

Rate of DNA juxtaposition from the +26° *parS* site. Related to Figure S10.

(A-B) Strain BWX3596 harboring a single *parS* site at +26° and an IPTG-inducible *gfp-parB* fusion as the sole source of the ParB protein. GFP-ParB was induced using 1 mM IPTG for indicated times and cells were harvested for Hi-C. The endpoints of DNA juxtaposition after GFP-ParB induction (from Fig. S10) were determined as described in Materials and Methods, using thresholds of 0.75σ (A) and 1.0σ (B). Left panels, binary file showing points with Hi-C interactions scores above the specified threshold (light green and yellow). Neighboring points that were separated by less than 10 bins (100 kb) were connected. The largest region of interconnected points (highlighted in yellow) was identified as the Hi-C enrichment region due to DNA juxtaposition. The endpoints of Hi-C enrichment regions were identified (white dotted lines). For visualization, these positions were marked with blue dotted lines on Hi-C contact maps on the right panels. The positions of the endpoint relative to +26° *parS* site were plotted on the graph at the bottom. The endpoint position close to the terminus (terminus-proximal) was given a positive value, and the endpoint position close to the origin (origin-proximal) a negative value. The rates and errors for the DNA juxtaposition were calculated from the slope of the line of best fit and the standard error of the regression, respectively. The rate of DNA incorporation into the zip-up on the origin-proximal side of *parS* was bi-phasic. We therefore calculated the rates independently using the first two time points and separately the last four time points. **(C)** Table of rates of DNA juxtaposition calculated from 4 different threshold values. The rates reported in the text correspond to the row highlighted in green (threshold= 1.0σ).

Table S1.

Strains used in this study

strain	genotype	reference	figure
BWX3352	<i>parSΔ9 no a.b., Δspo0J (remains wt parS at -1°)::spec, yvbJ::Pspank (optRBS) gfp-spo0J(ΔparS) (cat)</i>	this study	1, 4D
BWX3377	<i>parSΔ9 no a.b., -59° parS (loxP-kan-loxP)</i>	this study	2
BWX3270	<i>parSΔ9 no a.b., -94° parS no a.b.</i>	this study	2
BWX3381	<i>parSΔ9 no a.b., -117° parS (loxP-kan-loxP)</i>	this study	2
BWX3690	<i>parSΔ9 no a.b., -94° parS no a.b., amyE::Pspank (natRBS) gfp-smc (spec)</i>	this study	3
BWX3403	<i>parSΔ9 no a.b., +26° parS (loxP-kan-loxP)</i>	this study	4A-C
BWX3268	<i>parSΔ9 no a.b., -27° parS no a.b.</i>	this study	4A
PY79	<i>wild-type</i>	(25)	
AG1468	<i>Δspo0J (remains wt parS at -1°)::spec, trpC2, pheA1</i>	(38)	
BNS1615	<i>parSΔ7: spo0J (parSΔ), yycG (parSΔ), rocR (parSΔ), cotF (parSΔ), metS (parSΔ), ybbC(parSΔ), ydaD(parSΔ)</i>	N. Sullivan and D.Z.R unpublished	
BNS1657	<i>parSΔ8: spo0J (parSΔ), yycG (parSΔ), rocR (parSΔ), cotF (parSΔ), metS (parSΔ), ybbC(parSΔ), ydaD(parSΔ), nfrA(parSΔ)</i>	(14)	
BWX2423	<i>Δspo0J (ΔparS)::loxP-spec-loxP</i>	(39)	
BWX3198	<i>parSΔ9 loxp-kan-loxP</i>	(4)	
BWX3212	<i>parSΔ9 no a.b.</i>	(4)	
BWX3217	<i>parSΔ8., -94° parS loxP-kan-loxP</i>	(4)	
BWX3264	<i>parSΔ9 no a.b., -94° parS loxP-kan-loxP</i>	(4)	
BWX3370	<i>parSΔ9 no a.b., -1° parS no a.b.</i>	this study	
MF60	<i>rpoC-gfp (spec)</i>	(40)	

Table S2.

Plasmids used in this study

plasmid	description	reference
pKM287	<i>ytoI::Psmc-gfp-smc (erm)</i>	(14)
pWX589	<i>yvbJ::Pspank-gfp-parB (ΔparS) (cat)</i>	(41)
pWX707	<i>amyE::Pspank (natRBS) gfp-smc (spec)</i>	this study

Table S3.

Oligonucleotides used in this study. Restriction endonuclease sites are capitalized.

oligos	sequence	use
oWX438	gaccaggagcaactggtaac	universal
oWX439	tcctctgtccctcgctcag	universal
oWX507	cgtcttgaatttcaattttccc	BWX3370
oWX508	acccttgcaaaggctcactgggcgc	BWX3370
oWX517	tttGCATGCTactgaacgaatttttgttcc	pWX707
oWX536	gaaggcacgttttatggacatgg	BWX3370
oWX888	agaggtaaacgtaatgctcgaggcc	BWX3370
oWX889	tacgatccgcggtaagagggtcg	BWX3370
oWX1077	ctgagcgagggcagaaggatccaaaaccatctcgaaatgg	BWX3370
oWX1078	gttgcggcgtgtccctggcattttatgcgcggcgtggcgttgc	BWX3370
oWX1241	ctcgagtgtaacacgtgaaacatccctctgtccctcgctcag	universal
oWX1273	tgtctgaccgttagtcaagcgccgc	BWX3377
oWX1274	gttgcggcgtgtccctggcattttatgcgcggcgtggcgttgc	BWX3377
oWX1275	tgttcacgtgtaaactcgagttacactgtgattcatcatgt	BWX3377
oWX1276	cgccgggagccatcggttcaccc	BWX3377
oWX1277	gacaaggccgatccctgtccgc	BWX3377
oWX1278	cttaatcatcggtgtggcaaccgg	BWX3377
oWX1285	cagcagatccgttataatcatgg	BWX3381
oWX1286	gttgcggcgtgtccctggcatttgcacaatcaaaaaggcggactatgc	BWX3381
oWX1287	tgttcacgtgtaaacactcgagttacacagctgtgagggttttg	BWX3381
oWX1288	gtcagaagacgcgtatacgaggtgc	BWX3381
oWX1289	atacgcaggagagaggggagacag	BWX3381
oWX1290	gcgggaacattaaattgaggagg	BWX3381
oWX1291	tgttgtccggttttatctcacc	BWX3383
oWX1292	tgttcacgtgtaaactcgagtcacgtgtggcttaagatgtgc	BWX3383
oWX1293	gttgcggcgtgtccctggcattttatgcgcattttgtactgc	BWX3383
oWX1294	gaaacagaaggcgcgaatccgcgt	BWX3383
oWX1295	ggatcataaaattccggatttacggcc	BWX3383
oWX1296	gctgttaggaggcggttgagcag	BWX3383
oWX1336	ctacataaaaaatctggacggcgg	BWX3403
oWX1337	tgttcacgtgtaaacactcgagttatgaggataacgtgtgcaaaac	BWX3403
oWX1338	gttgcggcgtgtccctggcattttatgcgcattttgtactgc	BWX3403
oWX1339	ctactgtgattacaccctgtgtatgg	BWX3403
oWX1340	gcagaattcttcatgcagttcag	BWX3403
oWX1341	cggatcaatacagccaatatgcac	BWX3403
oWX1466	<u>tttCTAGAaggaggatcgctatgatgaaaggagaagaactttcac</u>	pWX707

References and Notes

1. M. Marbouty, A. Le Gall, D. I. Cattoni, A. Cournac, A. Koh, J.-B. Fiche, J. Mozziconacci, H. Murray, R. Koszul, M. Nollmann, Condensin- and replication-mediated bacterial chromosome folding and origin condensation revealed by Hi-C and super-resolution imaging. *Mol. Cell* **59**, 588–602 (2015). [doi:10.1016/j.molcel.2015.07.020](https://doi.org/10.1016/j.molcel.2015.07.020) [Medline](#)
2. N. Naumova, M. Imakaev, G. Fudenberg, Y. Zhan, B. R. Lajoie, L. A. Mirny, J. Dekker, Organization of the mitotic chromosome. *Science* **342**, 948–953 (2013). [doi:10.1126/science.1236083](https://doi.org/10.1126/science.1236083) [Medline](#)
3. A. L. Sanborn, S. S. P. Rao, S.-C. Huang, N. C. Durand, M. H. Huntley, A. I. Jewett, I. D. Bochkov, D. Chinnappan, A. Cutkosky, J. Li, K. P. Geeting, A. Gnirke, A. Melnikov, D. McKenna, E. K. Stamenova, E. S. Lander, E. L. Aiden, Chromatin extrusion explains key features of loop and domain formation in wild-type and engineered genomes. *Proc. Natl. Acad. Sci. U.S.A.* **112**, E6456–E6465 (2015). [doi:10.1073/pnas.1518552112](https://doi.org/10.1073/pnas.1518552112) [Medline](#)
4. X. Wang, T. B. K. Le, B. R. Lajoie, J. Dekker, M. T. Laub, D. Z. Rudner, Condensin promotes the juxtaposition of DNA flanking its loading site in *Bacillus subtilis*. *Genes Dev.* **29**, 1661–1675 (2015). [doi:10.1101/gad.265876.115](https://doi.org/10.1101/gad.265876.115) [Medline](#)
5. E. Alipour, J. F. Marko, Self-organization of domain structures by DNA-loop-extruding enzymes. *Nucleic Acids Res.* **40**, 11202–11212 (2012). [doi:10.1093/nar/gks925](https://doi.org/10.1093/nar/gks925) [Medline](#)
6. J. Dekker, L. Mirny, The 3D genome as moderator of chromosomal communication. *Cell* **164**, 1110–1121 (2016). [doi:10.1016/j.cell.2016.02.007](https://doi.org/10.1016/j.cell.2016.02.007) [Medline](#)
7. A. Goloborodko, M. V. Imakaev, J. F. Marko, L. Mirny, Compaction and segregation of sister chromatids via active loop extrusion. *eLife* **5**, e14864 (2016). [doi:10.7554/eLife.14864](https://doi.org/10.7554/eLife.14864) [Medline](#)
8. K. Nasmyth, Disseminating the genome: Joining, resolving, and separating sister chromatids during mitosis and meiosis. *Annu. Rev. Genet.* **35**, 673–745 (2001). [doi:10.1146/annurev.genet.35.102401.091334](https://doi.org/10.1146/annurev.genet.35.102401.091334) [Medline](#)
9. G. Fudenberg, M. Imakaev, C. Lu, A. Goloborodko, N. Abdennur, L. A. Mirny, Formation of chromosomal domains by loop extrusion. *Cell Reports* **15**, 2038–2049 (2016). [doi:10.1016/j.celrep.2016.04.085](https://doi.org/10.1016/j.celrep.2016.04.085) [Medline](#)
10. S. Gruber, J.-W. Veenings, J. Bach, M. Blettinger, M. Bramkamp, J. Errington, Interlinked sister chromosomes arise in the absence of condensin during fast replication in *B. subtilis*. *Curr. Biol.* **24**, 293–298 (2014). [doi:10.1016/j.cub.2013.12.049](https://doi.org/10.1016/j.cub.2013.12.049) [Medline](#)
11. X. Wang, O. W. Tang, E. P. Riley, D. Z. Rudner, The SMC condensin complex is required for origin segregation in *Bacillus subtilis*. *Curr. Biol.* **24**, 287–292 (2014). [doi:10.1016/j.cub.2013.11.050](https://doi.org/10.1016/j.cub.2013.11.050) [Medline](#)
12. A. M. Breier, A. D. Grossman, Whole-genome analysis of the chromosome partitioning and sporulation protein Spo0J (ParB) reveals spreading and origin-distal sites on the *Bacillus subtilis* chromosome. *Mol. Microbiol.* **64**, 703–718 (2007). [doi:10.1111/j.1365-2958.2007.05690.x](https://doi.org/10.1111/j.1365-2958.2007.05690.x) [Medline](#)

13. S. Gruber, J. Errington, Recruitment of condensin to replication origin regions by ParB/SpoOJ promotes chromosome segregation in *B. subtilis*. *Cell* **137**, 685–696 (2009). [doi:10.1016/j.cell.2009.02.035](https://doi.org/10.1016/j.cell.2009.02.035) [Medline](#)
14. N. L. Sullivan, K. A. Marquis, D. Z. Rudner, Recruitment of SMC by ParB-*parS* organizes the origin region and promotes efficient chromosome segregation. *Cell* **137**, 697–707 (2009). [doi:10.1016/j.cell.2009.04.044](https://doi.org/10.1016/j.cell.2009.04.044) [Medline](#)
15. L. Wilhelm, F. Bürmann, A. Minnen, H. C. Shin, C. P. Toseland, B. H. Oh, S. Gruber, SMC condensin entraps chromosomal DNA by an ATP hydrolysis dependent loading mechanism in *Bacillus subtilis*. *eLife* **4**, e06659 (2015). [doi:10.7554/eLife.06659](https://doi.org/10.7554/eLife.06659) [Medline](#)
16. A. Minnen, F. Bürmann, L. Wilhelm, A. Anchimiuk, M.-L. Diebold-Durand, S. Gruber, Control of Smc coiled coil architecture by the ATPase heads facilitates targeting to chromosomal ParB/*parS* and release onto flanking DNA. *Cell Reports* **14**, 2003–2016 (2016). [doi:10.1016/j.celrep.2016.01.066](https://doi.org/10.1016/j.celrep.2016.01.066) [Medline](#)
17. J. Stigler, G. O. Çamdere, D. E. Koshland, E. C. Greene, Single-molecule imaging reveals a collapsed conformational state for DNA-bound cohesin. *Cell Reports* **15**, 988–998 (2016). [doi:10.1016/j.celrep.2016.04.003](https://doi.org/10.1016/j.celrep.2016.04.003) [Medline](#)
18. P. Nicolas, U. Mäder, E. Dervyn, T. Rochat, A. Leduc, N. Pigeonneau, E. Bidnenko, E. Marchadier, M. Hoebeke, S. Aymerich, D. Becher, P. Bisicchia, E. Botella, O. Delumeau, G. Doherty, E. L. Denham, M. J. Fogg, V. Fromion, A. Goelzer, A. Hansen, E. Härtig, C. R. Harwood, G. Homuth, H. Jarmer, M. Jules, E. Klipp, L. Le Chat, F. Lecointe, P. Lewis, W. Liebermeister, A. March, R. A. T. Mars, P. Nannapaneni, D. Noone, S. Pohl, B. Rinn, F. Rügheimer, P. K. Sappa, F. Samson, M. Schaffer, B. Schwikowski, L. Steil, J. Stülke, T. Wiegert, K. M. Devine, A. J. Wilkinson, J. M. van Dijl, M. Hecker, U. Völker, P. Bessières, P. Noirot, Condition-dependent transcriptome reveals high-level regulatory architecture in *Bacillus subtilis*. *Science* **335**, 1103–1106 (2012). [doi:10.1126/science.1206848](https://doi.org/10.1126/science.1206848) [Medline](#)
19. T. B. Le, M. V. Imakaev, L. A. Mirny, M. T. Laub, High-resolution mapping of the spatial organization of a bacterial chromosome. *Science* **342**, 731–734 (2013). [doi:10.1126/science.1242059](https://doi.org/10.1126/science.1242059) [Medline](#)
20. J. E. Cabrera, D. J. Jin, The distribution of RNA polymerase in *Escherichia coli* is dynamic and sensitive to environmental cues. *Mol. Microbiol.* **50**, 1493–1505 (2003). [doi:10.1046/j.1365-2958.2003.03805.x](https://doi.org/10.1046/j.1365-2958.2003.03805.x) [Medline](#)
21. J. F. Marko, Micromechanical studies of mitotic chromosomes. *Chromosome Res.* **16**, 469–497 (2008). [doi:10.1007/s10577-008-1233-7](https://doi.org/10.1007/s10577-008-1233-7) [Medline](#)
22. T. R. Strick, T. Kawaguchi, T. Hirano, Real-time detection of single-molecule DNA compaction by condensin I. *Curr. Biol.* **14**, 874–880 (2004). [doi:10.1016/j.cub.2004.04.038](https://doi.org/10.1016/j.cub.2004.04.038) [Medline](#)
23. H. Kim, J. J. Loparo, Multistep assembly of DNA condensation clusters by SMC. *Nat. Commun.* **7**, 10200 (2016). [doi:10.1038/ncomms10200](https://doi.org/10.1038/ncomms10200) [Medline](#)
24. Y. M. Soh, F. Bürmann, H.-C. Shin, T. Oda, K. S. Jin, C. P. Toseland, C. Kim, H. Lee, S. J. Kim, M.-S. Kong, M.-L. Durand-Diebold, Y.-G. Kim, H. M. Kim, N. K. Lee, M. Sato,

- B.-H. Oh, S. Gruber, Molecular basis for SMC rod formation and its dissolution upon DNA binding. *Mol. Cell* **57**, 290–303 (2015). [doi:10.1016/j.molcel.2014.11.023](https://doi.org/10.1016/j.molcel.2014.11.023) [Medline](#)
25. P. J. Youngman, J. B. Perkins, R. Losick, Genetic transposition and insertional mutagenesis in *Bacillus subtilis* with *Streptococcus faecalis* transposon Tn917. *Proc. Natl. Acad. Sci. U.S.A.* **80**, 2305–2309 (1983). [doi:10.1073/pnas.80.8.2305](https://doi.org/10.1073/pnas.80.8.2305) [Medline](#)
26. C. R. Harwood, S. M. Cutting, *Molecular Biological Methods for Bacillus* (Wiley, 1990).
27. M. Imakaev, G. Fudenberg, R. P. McCord, N. Naumova, A. Goloborodko, B. R. Lajoie, J. Dekker, L. A. Mirny, Iterative correction of Hi-C data reveals hallmarks of chromosome organization. *Nat. Methods* **9**, 999–1003 (2012). [doi:10.1038/nmeth.2148](https://doi.org/10.1038/nmeth.2148) [Medline](#)
28. P. J. Rousseeuw, C. Croux, Alternatives to the median absolute deviation. *J. Am. Stat. Assoc.* **88**, 1273–1283 (1993). [doi:10.1080/01621459.1993.10476408](https://doi.org/10.1080/01621459.1993.10476408)
29. J. C. Lindow, M. Kuwano, S. Moriya, A. D. Grossman, Subcellular localization of the *Bacillus subtilis* structural maintenance of chromosomes (SMC) protein. *Mol. Microbiol.* **46**, 997–1009 (2002). [doi:10.1046/j.1365-2958.2002.03235.x](https://doi.org/10.1046/j.1365-2958.2002.03235.x) [Medline](#)
30. D. C. Lin, P. A. Levin, A. D. Grossman, Bipolar localization of a chromosome partition protein in *Bacillus subtilis*. *Proc. Natl. Acad. Sci. U.S.A.* **94**, 4721–4726 (1997). [doi:10.1073/pnas.94.9.4721](https://doi.org/10.1073/pnas.94.9.4721) [Medline](#)
31. D. Z. Rudner, P. Fawcett, R. Losick, A family of membrane-embedded metalloproteases involved in regulated proteolysis of membrane-associated transcription factors. *Proc. Natl. Acad. Sci. U.S.A.* **96**, 14765–14770 (1999). [doi:10.1073/pnas.96.26.14765](https://doi.org/10.1073/pnas.96.26.14765) [Medline](#)
32. P. A. Levin, R. Losick, Transcription factor Spo0A switches the localization of the cell division protein FtsZ from a medial to a bipolar pattern in *Bacillus subtilis*. *Genes Dev.* **10**, 478–488 (1996). [doi:10.1101/gad.10.4.478](https://doi.org/10.1101/gad.10.4.478) [Medline](#)
33. M. Fujita, Temporal and selective association of multiple sigma factors with RNA polymerase during sporulation in *Bacillus subtilis*. *Genes Cells* **5**, 79–88 (2000). [doi:10.1046/j.1365-2443.2000.00307.x](https://doi.org/10.1046/j.1365-2443.2000.00307.x) [Medline](#)
34. H. El Sayyed, L. Le Chat, E. Lebailly, E. Vickridge, C. Pages, F. Cornet, M. Cosentino Lagomarsino, O. Espéli, Mapping Topoisomerase IV binding and activity sites on the *E. coli* genome. *PLOS Genet.* **12**, e1006025 (2016). [doi:10.1371/journal.pgen.1006025](https://doi.org/10.1371/journal.pgen.1006025) [Medline](#)
35. S. Nolivos, A. L. Upton, A. Badrinarayanan, J. Müller, K. Zawadzka, J. Wiktor, A. Gill, L. Arciszewska, E. Nicolas, D. Sherratt, MatP regulates the coordinated action of topoisomerase IV and MukBEF in chromosome segregation. *Nat. Commun.* **7**, 10466 (2016). [doi:10.1038/ncomms10466](https://doi.org/10.1038/ncomms10466) [Medline](#)
36. L. Teytelman, D. M. Thurtle, J. Rine, A. van Oudenaarden, Highly expressed loci are vulnerable to misleading ChIP localization of multiple unrelated proteins. *Proc. Natl. Acad. Sci. U.S.A.* **110**, 18602–18607 (2013). [doi:10.1073/pnas.1316064110](https://doi.org/10.1073/pnas.1316064110) [Medline](#)

37. J. D. McGhee, P. H. von Hippel, Formaldehyde as a probe of DNA structure. 4. Mechanism of the initial reaction of formaldehyde with DNA. *Biochemistry* **16**, 3276–3293 (1977). [doi:10.1021/bi00634a002](https://doi.org/10.1021/bi00634a002) [Medline](#)
38. K. Ireton, N. W. Gunther 4th, A. D. Grossman, *spo0J* is required for normal chromosome segregation as well as the initiation of sporulation in *Bacillus subtilis*. *J. Bacteriol.* **176**, 5320–5329 (1994). [doi:10.1128/jb.176.17.5320-5329.1994](https://doi.org/10.1128/jb.176.17.5320-5329.1994) [Medline](#)
39. T. G. Graham, X. Wang, D. Song, C. M. Etson, A. M. van Oijen, D. Z. Rudner, J. J. Loparo, ParB spreading requires DNA bridging. *Genes Dev.* **28**, 1228–1238 (2014). [doi:10.1101/gad.242206.114](https://doi.org/10.1101/gad.242206.114) [Medline](#)
40. I. A. Berlitzky, A. Rovinsky, S. Ben-Yehuda, Spatial organization of a replicating bacterial chromosome. *Proc. Natl. Acad. Sci. U.S.A.* **105**, 14136–14140 (2008). [doi:10.1073/pnas.0804982105](https://doi.org/10.1073/pnas.0804982105) [Medline](#)
41. C. P. Broedersz, X. Wang, Y. Meir, J. J. Loparo, D. Z. Rudner, N. S. Wingreen, Condensation and localization of the partitioning protein ParB on the bacterial chromosome. *Proc. Natl. Acad. Sci. U.S.A.* **111**, 8809–8814 (2014). [doi:10.1073/pnas.1402529111](https://doi.org/10.1073/pnas.1402529111) [Medline](#)